

# Titanium oxynitride electron-selective contact for crystalline silicon solar cells

Cite as: Appl. Phys. Lett. **127**, 153901 (2025); doi: [10.1063/5.0287987](https://doi.org/10.1063/5.0287987)

Submitted: 28 June 2025 · Accepted: 25 September 2025 ·

Published Online: 13 October 2025



View Online



Export Citation



CrossMark

Wenhai Li, Kun Gao, Jun Zhou, Peng Xie, Gege Yan, Xinyao Sun, and Xinbo Yang <sup>a)</sup>

## AFFILIATIONS

College of Energy, Soochow University, Suzhou 215006, China

<sup>a)</sup>Author to whom correspondence should be addressed: [xbyang@suda.edu.cn](mailto:xbyang@suda.edu.cn)

## ABSTRACT

Wide-bandgap metal compound-based carrier-selective contacts are being intensively developed to mitigate the carrier recombination losses at the contact regions of crystalline silicon (*c*-Si) solar cells. In this work, magnetron sputtered titanium oxynitride ( $\text{TiO}_x\text{N}_y$ ) is exploited as an electron-selective contact for *c*-Si solar cells. We investigate the effect of various deposition parameters ( $\text{N}_2$  concentration, power, and pressure) on the optoelectronic properties of  $\text{TiO}_x\text{N}_y$  films. The optimized  $\text{TiO}_x\text{N}_y$  film features a low resistivity of  $9 \times 10^{-4} \Omega \text{ cm}$  and high transmittance. The surface passivation and contact resistivity of  $\text{TiO}_x\text{N}_y$  films on *c*-Si were also investigated. The results demonstrate that  $\text{TiO}_x\text{N}_y$  can effectively serve as an electron-selective contact for *c*-Si solar cells due to its low WF (4.15 eV) and low contact resistivity of  $9.4 \text{ m}\Omega \text{ cm}^2$  on *c*-Si. By implementing a full-area  $\text{TiO}_x\text{N}_y$  rear contact, a champion efficiency of 20.2% is obtained on the n-type *c*-Si solar cell, representing an absolute efficiency gain of 4.4%.

Published under an exclusive license by AIP Publishing. <https://doi.org/10.1063/5.0287987>

Crystalline silicon (*c*-Si) solar cells dominate the photovoltaic (PV) market due to their high efficiency and reliability. Currently, *c*-Si solar cells with passivating contacts have replaced the dominant role of passivated emitter and rear contact (PERC) cells.<sup>1,2</sup> The advanced passivating contacts based on doped silicon layers (e.g., tunnel oxide passivating contact TOPCon and silicon heterojunction technology SHJ) significantly reduce carrier recombination at both the contact and non-contact regions, thereby enhancing both the open-circuit voltage ( $V_{oc}$ ) and overall power conversion efficiency (PCE).<sup>3–5</sup> Specifically, ultrahigh PCEs of 27.3%<sup>6</sup> and 26.4%<sup>6</sup> have been achieved on SHJ and TOPCon solar cells, respectively. Nevertheless, the high parasitic absorption of doped silicon layers impedes further PCE improvement of SHJ and TOPCon solar cells.

As a substitute, wide-bandgap metal compound-based carrier-selective contacts have gained significant attention due to the simple deposition process and minimal parasitic absorption.<sup>7,8</sup> Typically, metal compounds featuring a low work function (e.g.,  $\text{TiO}_x$ ,<sup>9</sup>  $\text{ZnO}_x$ ,<sup>10</sup>  $\text{TaO}_x$ ,<sup>11</sup>  $\text{MgO}_x$ ,<sup>12,13</sup>  $\text{Nd}_2\text{O}_3-x$ ,<sup>14</sup>  $\text{SrO}_x$ ,<sup>15</sup>  $\text{SrF}_x$ ,<sup>16</sup>  $\text{AlF}_x$ ,<sup>17</sup>  $\text{MgF}_x$ ,<sup>18</sup>  $\text{TiN}_x$ ,<sup>19</sup>  $\text{TaN}_x$ ,<sup>20</sup> AZO,<sup>21</sup>  $\text{MgO}_x/\text{AZO}$ ,<sup>22</sup> and  $\text{BaO}_x\text{F}_y/\text{LiF}$ <sup>23</sup>) serve as electron-selective contacts (ESCs). In contrast, high-work function materials (e.g.,  $\text{MoO}_x$ ,<sup>24,25</sup>  $\text{VO}_x$ ,<sup>26,27</sup>  $\text{WO}_x$ ,<sup>28</sup>  $\text{NiO}_x$ ,<sup>29</sup> and  $\text{Cu}_2\text{O}$ <sup>30</sup>) can be developed as hole-selective contacts (HSCs). Up to this point, champion PCEs of 24.3%<sup>21</sup> and 23.8%<sup>31</sup> have been obtained on *c*-Si solar cells featuring electron-selective contact of  $\text{SiO}_2/\text{ZnO}$  and hole-selective contact of

$\text{a-Si:H/MoO}_x$  respectively. By integrating the front  $\text{MgO}_x/\text{AZO}$  ESC and rear  $\text{VO}_x$  HSC,<sup>22</sup> a high PCE of 22.8% was achieved on *c*-Si solar cells with both-side asymmetric hetero-contacts. Although these studies have demonstrated the immense potential of these materials, the performance of *c*-Si solar cells remains inferior to that of silicon-based passivating contacts, primarily due to the poor surface passivation and stability. Therefore, the development of new metal compound material that simultaneously provides excellent surface passivation and low contact resistivity is crucial for further enhancing the performance of *c*-Si solar cells.

Recently, due to their appropriate work function and excellent conductivity, metal (oxy)nitrides have been investigated as potential ESCs for *c*-Si solar cells. For instance,  $\text{TaN}_x$ ,<sup>20</sup>  $\text{TiN}_x$ ,<sup>19</sup> and  $\text{ZrN}$ <sup>32</sup> demonstrated good electron selectivity and excellent stability, achieving moderate PCEs of 20.1%, 20.0%, and 19.7% on *c*-Si solar cells, respectively. However, it was found that high carrier concentration in metal nitrides can result in severe parasitic absorption. Yang *et al.* deposited  $\text{TiO}_x\text{N}_y$  films by ALD and developed  $\text{a-Si:H}/\text{TiO}_x\text{N}_y$  stack as an efficient ESC for *c*-Si solar cells,<sup>33</sup> achieving a high PCE of 22.3%. Yu *et al.* reported TiN electron-selective contact deposited by sputtering using a TiN ceramic target, achieving a much lower PCE of 18.2% on *c*-Si solar cells.<sup>34</sup> Compared to ALD, reactive sputtering offers a higher deposition rate and is more conducive to the flexible control of the composition of oxynitride films. In this paper, we deposited  $\text{TiO}_x\text{N}_y$  films by

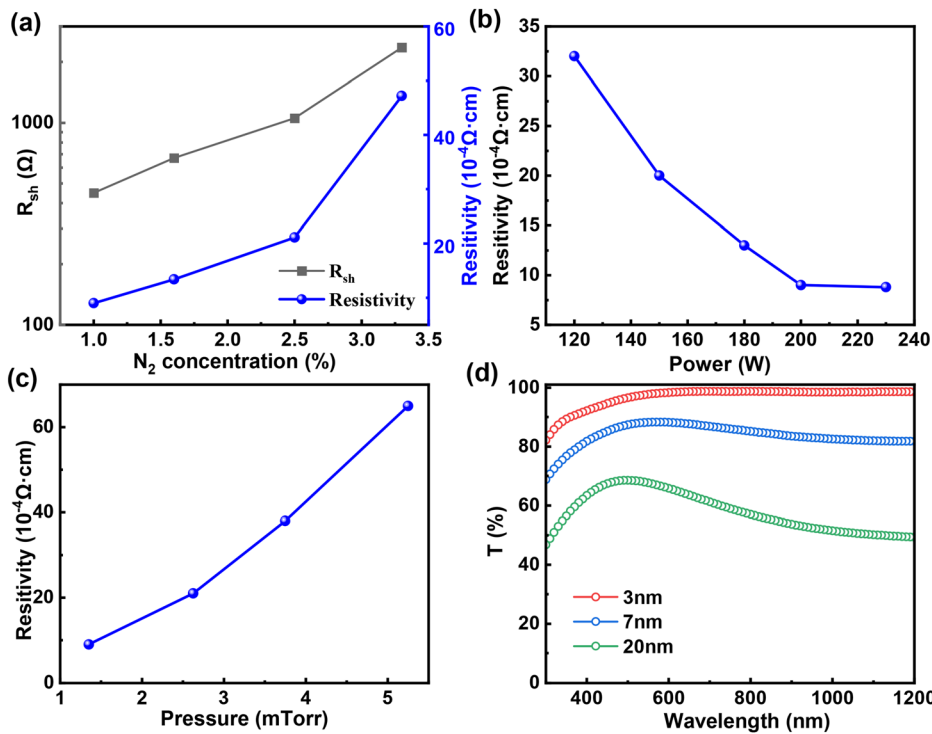


FIG. 1. (a)  $R_{sh}$  and resistivity of  $\text{TiO}_x\text{N}_y$  films ( $\sim 20$  nm) as a function of nitrogen concentration. Dependence of resistivity on (b) power and (c) pressure. (d) Optical transmission spectra of  $\text{TiO}_x\text{N}_y$  films of different thicknesses.

18 October 2025 14:38:35

reactive sputtering using a titanium target and optimized their opto-electronic properties. The element composition of  $\text{TiO}_x\text{N}_y$  films was analyzed, and the passivation and contact performance of  $\text{TiO}_x\text{N}_y$  on n-type *c*-Si were also investigated and optimized. Ultimately, by implementing the single-layer electron-selective  $\text{TiO}_x\text{N}_y$  contact, a PCE of 20.2% is achieved on *c*-Si.

The  $\text{TiO}_x\text{N}_y$  films were deposited using RF magnetron sputtering with varying nitrogen concentrations, powers, and chamber pressures. We first investigated the effect of nitrogen concentration on the opto-electronic properties of the films. Figure 1(a) shows the dependence of sheet resistance ( $R_{sh}$ ) and the corresponding resistivity of  $\text{TiO}_x\text{N}_y$  on the nitrogen concentration. The  $R_{sh}$  rises rapidly as the nitrogen concentration increases under the same thickness ( $\sim 20$  nm), and the resistivity follows a similar trend. A lowest  $R_{sh}$  of  $450 \Omega/\text{sq}$  is obtained at the lowest nitrogen concentration of 1% and this minimum value is slightly higher than that of TiN ( $\sim 250 \Omega/\text{sq}$ ) reported by Yang *et al.*<sup>19</sup> So the  $\text{TiO}_x\text{N}_y$  films discussed in this study were deposited under a constant nitrogen concentration of 1.0%, unless otherwise specified. Figure 1(b) illustrates the resistivity of  $\text{TiO}_x\text{N}_y$  films as a function of power. With increasing power, the resistivity of the  $\text{TiO}_x\text{N}_y$  film decreases continuously, which can be attributed to the improved film density under high plasma energy. As the power increases from 120 to 200 W, the resistivity significantly decreases from  $3.3 \times 10^{-3}$  to  $9 \times 10^{-4} \Omega \cdot \text{cm}$ . Further increasing the power to 230 W results in a slight decrease in resistivity to  $8.8 \times 10^{-4} \Omega \cdot \text{cm}$ . In contrast, as shown in Figure 1(c), the effect of chamber pressure exhibits an opposite trend: as the pressure increases, the resistivity increases significantly. Therefore, high power (200 W) and low pressure (1.35 mTorr) are more favorable for depositing  $\text{TiO}_x\text{N}_y$  films with high conductivity. Additionally, we compared the optical transmission spectra of  $\text{TiO}_x\text{N}_y$

films with varying thicknesses. As shown in Figure 1(d), the transmittance of  $\text{TiO}_x\text{N}_y$  films decreases dramatically with increasing thickness. At a thickness of 3 nm, the  $\text{TiO}_x\text{N}_y$  film shows an average transmittance of 97.7%, whereas it decreases to 60.6% for 20 nm. The reduction in long-wavelength transmittance with increasing  $\text{TiO}_x\text{N}_y$  film thickness is probably ascribed to the free carrier absorption due to its quasi-metallic property and high carrier density for thick  $\text{TiO}_x\text{N}_y$  film.

High-resolution x-ray photoelectron spectroscopy (XPS) was employed to determine the chemical composition of  $\text{TiO}_x\text{N}_y$  films. Figure 2(a) displays the XPS core-level spectrum of Ti 2p in the film, which can be deconvoluted into three doublets between Ti 2p<sub>3/2</sub> and Ti 2p<sub>1/2</sub>. The Ti 2p<sub>3/2</sub> peak located at 455.1 eV and the 2p<sub>1/2</sub> peak located at 461.1 eV correspond to the Ti-N bond, the 2p<sub>3/2</sub> peak located at 456.7 eV and the 2p<sub>1/2</sub> peak located at 463.1 eV correspond to the Ti-ON bond, and the 2p<sub>3/2</sub> peak located at 458.3 eV and the

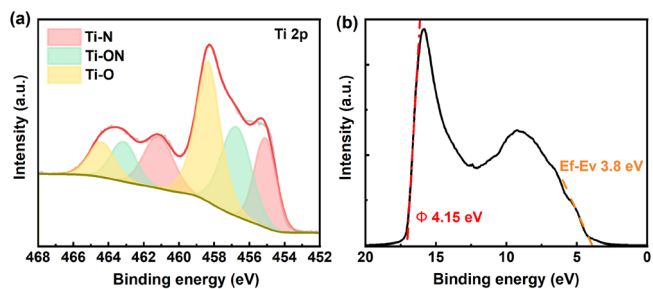


FIG. 2. (a) XPS core-level spectrum of Ti 2p and (b) UPS spectrum for  $\text{TiO}_x\text{N}_y$  films.

$2p_{1/2}$  peak located at 464.4 eV correspond to the Ti-O bond.<sup>34,35</sup> The calculated percentages of  $TiN_x$ ,  $TiO_xN_y$ , and  $TiO_x$  are 23.6%, 32.7%, and 43.7%, respectively, so we define the film with a non-stoichiometric chemical formula  $TiO_xN_y$ . The residual oxygen in the chamber during the deposition process results in the formation of  $TiO_xN_y$  and  $TiO_x$ . The optical bandgap of  $TiO_xN_y$  was determined to be approximately 3.42 eV, obtained via ultraviolet-visible (UV-vis) spectroscopy using  $T_{auc}$  plots (Fig. S1), which is higher than that of 3.2 eV of  $TiN_x$ .<sup>19</sup> The incorporation of oxygen achieves a balance between the properties of high transparency of  $TiO_2$ <sup>9</sup> and high conductivity of  $TiN_x$ .<sup>19</sup> Therefore, controlling the oxygen concentration during the deposition process is also crucial. As shown in Fig. 2(b), the work function, calculated from the onset of the ultraviolet photoelectron spectroscopy (UPS) spectrum, is determined to be 4.15 eV. The  $E_F-E_V$  value (3.8 eV) is obtained from the cutoff in the UPS spectrum, indicating that the Fermi level is close to the conduction band, which is characteristic of n-type semiconductors.

The contact resistivity ( $\rho_c$ ) of the n-Si/ $TiO_xN_y$ /Al heterocontacts was measured using the transfer-length method (TLM),<sup>36</sup> as shown in Fig. 3(a). By measuring the resistance at different electrode spacings and fitting the linear relationship between resistance and spacing, the  $\rho_c$  of the heterocontact can be extracted. Figure 3(b) shows the dark J-V curves of Al/Si Schottky structures, with and without  $TiO_xN_y$  interlayer on the different c-Si substrates. The direct n-Si/Al contact exhibits typical Schottky behavior (blue line), which can be attributed to the presence of a large Schottky barrier at the interface, hindering the flow of electrons from the n-Si. The insertion of the  $TiO_xN_y$  interlayer alleviates the Schottky behavior, resulting in Ohmic contact characteristics in the J-V curve (red line). In contrast, the opposite effect is observed on the p-Si substrate. The results

indicate that the  $TiO_xN_y$ /Si heterojunction can effectively reduce the Schottky barrier height of n-Si/Al and block holes effectively. Figure 3(c) shows the dark J-V curves under different spacings, a lowest  $\rho_c$  of 9.4 m $\Omega$  cm<sup>2</sup> is extracted with 3 nm  $TiO_xN_y$ . The  $\rho_c$  outperforms that of other reported electron-selective contacts, including sputtered  $TiN_x$ <sup>19</sup> (16.4 m $\Omega$  cm<sup>2</sup>) and ALD  $TaN_x$ <sup>20</sup> ( $\sim$ 42 m $\Omega$  cm<sup>2</sup>). Figure 3(d) displays the effect of  $TiO_xN_y$  thickness on the  $\rho_c$  of n-Si/ $TiO_xN_y$ /Al heterocontacts. The  $\rho_c$  increases from 9.4 to 113 m $\Omega$  cm<sup>2</sup> as the thickness increases from 3 to 8 nm, which can be ascribed to enhanced tunneling resistance due to increased bulk resistance.

Passivation quality is another critical parameter for high-quality passivating contacts, and the implied open-circuit voltage ( $iV_{oc}$ ) measured by the Sinton Lifetime Tester can effectively reflect this performance. Figures S2(a) and S2(c) illustrate the  $iV_{oc}$  and effective minority carrier lifetimes ( $\tau_{eff}$ ) of n-Si passivated by single-layer  $TiO_xN_y$  (3–8 nm) as a function of annealing temperature. As the annealing temperature increases from 200 to 600 °C, the  $iV_{oc}$  of  $TiO_xN_y$  passivated n-Si fluctuates around 540 mV and the  $\tau_{eff}$  of  $TiO_xN_y$  passivated n-Si fluctuates around 2  $\mu$ s, indicating a lower passivation level. This demonstrates that the single-layer  $TiO_xN_y$  thin films cannot offer effective passivation. The thermally grown  $SiO_x$  layer was proven to be effective in promoting surface passivation for  $ZnO^{21}$  and  $TiO_2$ <sup>9</sup> passivating contacts, and we tried to implement the tunnel  $SiO_2$  (0.7 nm) into the  $TiO_xN_y$  contact as well. Unfortunately, we found that  $SiO_x$  passivation interlayer cannot improve the passivation quality of  $TiO_xN_y$  contact, neither before annealing nor after annealing, as shown in Figs. S2(b) and S2(d). The poor passivation quality might be attributed to sputtering damage on the c-Si substrate, which induces surface defects that cannot be cured by annealing.

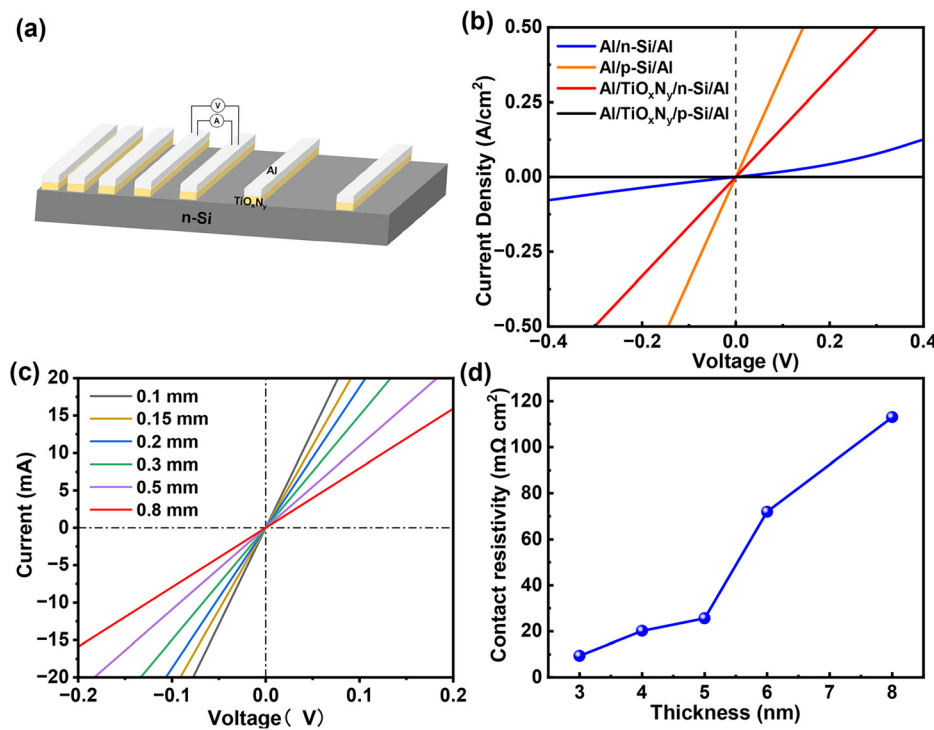


**FIG. 3.** (a) Schematic of the TLM structure. (b) Dark J-V curves of Al/Si Schottky structures with and without a  $TiO_xN_y$  interlayer (3 nm). (c) Dark J-V curves of n-Si/ $TiO_xN_y$ /Al heterocontact under different spacings. (d) Dependence of  $\rho_c$  on the  $TiO_xN_y$  film thickness of n-Si/ $TiO_xN_y$ /Al heterocontacts.

To verify its electron-selective contact performance, we designed and fabricated n-Si solar cells with full-area  $\text{TiO}_{x}\text{N}_y$  rear contacts, as shown in Fig. 4(a). The cell features a boron diffused  $p^{+}$  emitter on textured random pyramids that are passivated by  $\text{Al}_2\text{O}_3/\text{SiN}_x$  stack on the front side and a rear full-area  $\text{TiO}_{x}\text{N}_y$  electron-selective contact (3 nm) capped with thermally evaporated Al electrodes. Figure 4(b) shows the  $J$ - $V$  curves of the n-Si solar cells with and without  $\text{TiO}_{x}\text{N}_y$ . The control device with a simple Al rear contact exhibits a low  $V_{oc}$  of 555 mV and a fill factor (FF) of 75.1%, resulting in a low PCE of 15.8%, which can be ascribed to the high carrier recombination and high contact resistance at the rear side. The device performance was significantly improved after the insertion of a 3 nm  $\text{TiO}_{x}\text{N}_y$  interlayer, owing to the reduced carrier recombination and decreased contact resistivity. The champion device achieved a PCE of 20.2% ( $V_{oc}$  619 mV,  $J_{sc}$  39.4 mA/cm<sup>2</sup>, and FF 82.9%), which is higher than that of ALD  $\text{TaN}_x$ <sup>20</sup>, sputtered  $\text{TiNx}$ ,<sup>19</sup> and sputtered  $\text{ZrN}$ <sup>32</sup> contacts. The PCE is mainly limited by a relatively low  $V_{oc}$  which is consistent with the poor surface passivation of  $\text{TiO}_{x}\text{N}_y$ .

Figure 4(c) displays the external quantum efficiency (EQE) spectra of the devices with and without a  $\text{TiO}_{x}\text{N}_y$  interlayer. Both cells show the same front structure, displaying minimal variation in the EQE in the short-wavelength range (<800 nm). However, in the long-wavelength range (>800 nm), the EQE is significantly improved after the introduction of a thin  $\text{TiO}_{x}\text{N}_y$  interlayer, confirming that the n-Si/ $\text{TiO}_{x}\text{N}_y$  heterojunction can effectively reduce carrier recombination at the rear side. Although the improved EQE suggests an increase in the effective minority carrier diffusion length, the corresponding enhancement in  $V_{oc}$  does not result solely from an extended carrier lifetime. Instead, it arises from the mitigation of metal-induced gap states

on c-Si and the subsequent de-pinning of the Fermi level.<sup>37</sup> The calculated  $J_{sc}$  for the champion device, obtained by integrating the product of EQE and AM1.5 spectrum and correcting for the approximate contact fraction, is shown to be 39.3 mA/cm<sup>2</sup>, which is in good agreement with the measured  $J_{sc}$  value. We re-introduced the  $\text{SiO}_x$  passivation layer to investigate its impact on device performance. Unfortunately, the device performance decreases, resulting from slightly reduced  $V_{oc}$  and FF, as shown in Fig. S3. The growth method and thickness of the  $\text{SiO}_x$  layer are crucial for its quality and can significantly impact the passivating contact. Therefore, further optimizing the  $\text{SiO}_x$  deposition process is key to utilizing it as a passivation layer in future applications. Figures 4(d) and S4 show the statistical distribution of photovoltaic parameters of seven devices with  $\text{TiO}_{x}\text{N}_y$  contacts and three control devices, evaluating the reliability of n-Si cells with  $\text{TiO}_{x}\text{N}_y$  contacts.

Finally, we investigate the environmental and thermal stability of the c-Si solar cells with  $\text{TiO}_{x}\text{N}_y$  contact. Figure 5(a) shows the photovoltaic parameters of the best n-Si cell with  $\text{TiO}_{x}\text{N}_y$  contact after being stored in air for 40 days (25–30 °C, 40%–50% humidity). A slight decrease in the PCE (~3.6% relatively) can be observed, due to the increased  $\rho_c$  of n-Si/ $\text{TiO}_{x}\text{N}_y$ /Al (Fig. S5), probably ascribed to the undesirable interface reaction between  $\text{TiO}_{x}\text{N}_y$  and Al, along with the oxidation of the Ag electrode for the unencapsulated devices, both of which increase the series resistance. Figure 5(b) displays the thermal stability of the device, featuring a negligible PCE degradation up to 400 °C. With further increases to 500 °C, the PCE reduces significantly. Figure S6 shows the change in  $V_{oc}$ , FF, and  $J_{sc}$  of the best device as a function of the forming gas annealing at different temperatures for 15 min. The  $V_{oc}$  reduction might be attributed to the degradation of the front  $\text{Al}_2\text{O}_3/\text{SiN}_x$  passivation, which was believed to be stable up to

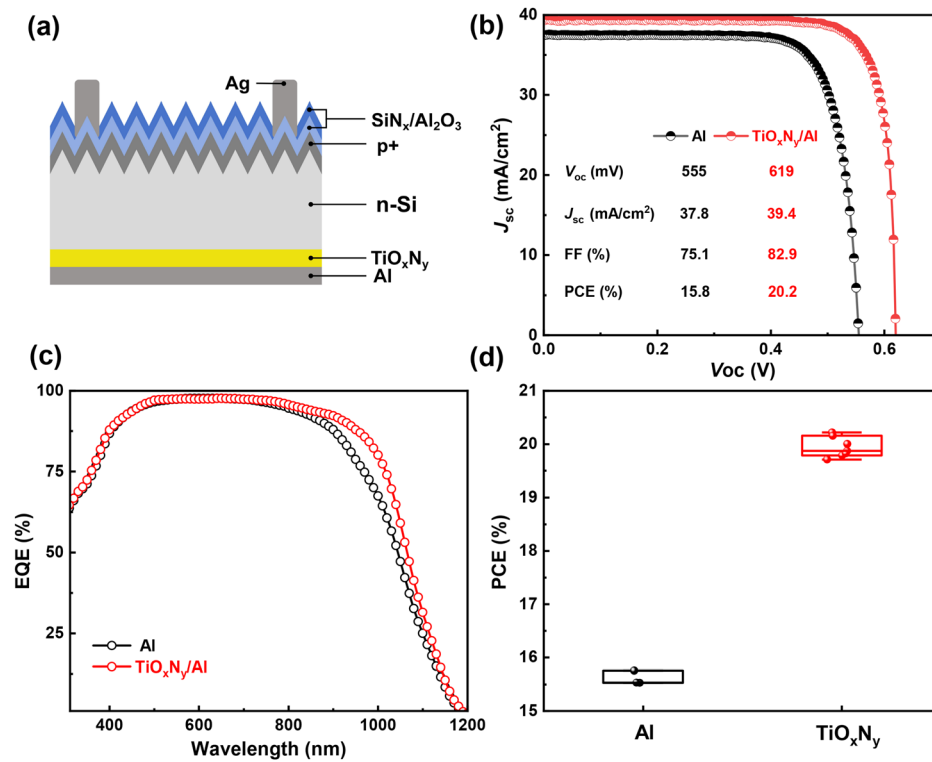
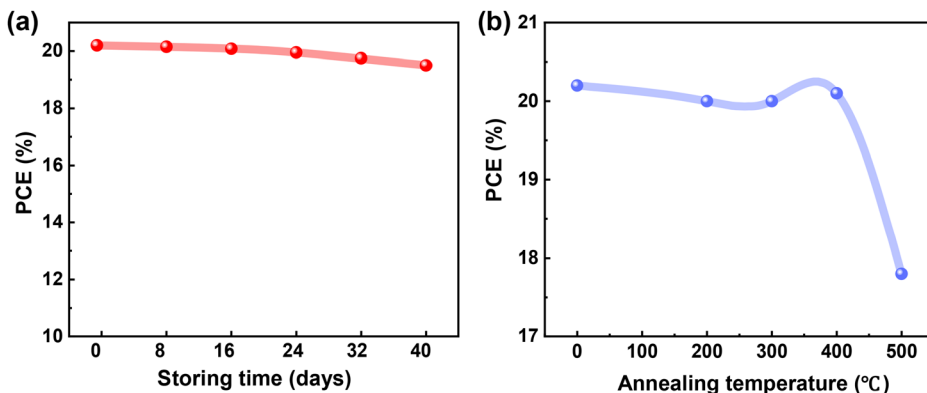


FIG. 4. (a) A schematic illustration of the n-Si solar cell with full-area  $\text{TiO}_{x}\text{N}_y$  contact. (b) Light J-V curves and photovoltaic parameters. (c) EQE of the cells with and without  $\text{TiO}_{x}\text{N}_y$  contact. (d) Statistical distribution of the PCE for n-Si cells with different rear contacts, including three control cells with Al contact and seven cells with  $\text{TiO}_{x}\text{N}_y$  contacts.



**FIG. 5.** (a) The environmental stability in air of c-Si solar cells with  $\text{TiO}_x\text{N}_y$  electron-selective contact. (b) The thermal stability of c-Si solar cells with  $\text{TiO}_x\text{N}_y$  electron-selective contact.

425 °C.<sup>38</sup> The FF degradation might be ascribed to the increased contact resistivity at the rear  $\text{TiO}_x\text{N}_y$  contact, which probably reacts with the Al electrode. Therefore, the device degradation stems from the deterioration of both the front and rear contacts under high temperatures.

In conclusion, we have developed  $\text{TiO}_x\text{N}_y$  electron-selective contacts for c-Si solar cells utilizing magnetron sputtering. The optoelectronic performance and elemental composition of  $\text{TiO}_x\text{N}_y$  films, as well as their contact properties on n-Si and device performance, are investigated and optimized. The  $\text{TiO}_x\text{N}_y$  films exhibit a low WF of 4.15 eV and a wide bandgap of 3.42 eV. The n-Si/ $\text{TiO}_x\text{N}_y$ /Al hetero-contact demonstrated hole-blocking behavior with a very low contact resistivity of 9.4 mΩ cm<sup>2</sup>. The  $\text{TiO}_x\text{N}_y$  contact was integrated into the c-Si solar cell, achieving an improved efficiency of 20.2%. The insufficient surface passivation limits the device efficiency; thus, further improvement is necessary. This work broadens the application of transition-metal oxynitride passivating contact for c-Si solar cells.

See the [supplementary material](#) for additional data on specific experimental section and data.

The authors acknowledge the financial support from the National Natural Science Foundation of China (No. 62174114), the National Key R&D Program of China (No. 2022YFB4200203), and the Department of Science and Technology of Jiangsu Province (Nos. BE2022027, BE2022036, and BE2022023).

## AUTHOR DECLARATIONS

### Conflict of Interest

The authors have no conflicts to disclose.

### Author Contributions

**Wenqiao Li:** Data curation (equal); Formal analysis (equal); Visualization (equal); Writing – original draft (lead); Writing – review & editing (equal). **Kun Gao:** Formal analysis (equal); Methodology (equal); Writing – review & editing (equal). **Jun Zhou:** Writing – review & editing (equal). **Peng Xie:** Writing – review & editing (equal). **Gege Yan:** Writing – review & editing (equal). **Xinyao Sun:** Writing – review & editing (equal). **Xinbo Yang:** Conceptualization (equal); Funding acquisition (equal); Resources (equal); Supervision (equal); Writing – review & editing (equal).

## DATA AVAILABILITY

The data that support the findings of this study are available from the corresponding author upon reasonable request.

## REFERENCES

- <sup>1</sup>M. Hermle, F. Feldmann, M. Bivour, J. C. Goldschmidt, and S. W. Glunz, *Appl. Phys. Rev.* **7**(2), 021305 (2020).
- <sup>2</sup>T. G. Allen, J. Bullock, X. Yang, A. Javey, and S. De Wolf, *Nat. Energy* **4**, 914–928 (2019).
- <sup>3</sup>Y. Liu, Y. Li, Y. Wu, G. Yang, L. Mazzarella, P. Procel-Moya, A. C. Tamboli, K. Weber, M. Boccard, O. Isabella, X. Yang, and B. Sun, *Mater. Sci. Eng.: R: Rep.* **142**, 100579 (2020).
- <sup>4</sup>M. Tanaka, M. Taguchi, T. Matsuyama, T. Sawada, S. Tsuda, S. Nakano, H. Hanafusa, and Y. Kuwano, *Jpn. J. Appl. Phys., Part 1* **31**, 3518–3522 (1992).
- <sup>5</sup>F. Feldmann, M. Bivour, C. Reichel, M. Hermle, and S. W. Glunz, *Sol. Energy Mater. Sol. Cells* **120**, 270–274 (2014).
- <sup>6</sup>M. A. Green, E. D. Dunlop, M. Yoshita, N. Kopidakis, K. Bothe, G. Siefer, X. Hao, and J. Y. Jiang, *Prog. Photovoltaics Res. Appl.* **33**(1), 3–15 (2024).
- <sup>7</sup>J. Melskens, B. W. H. van de Loo, B. Macco, L. E. Black, S. Smit, and W. M. M. Kessels, *IEEE J. Photovoltaics* **8**(2), 373–388 (2018).
- <sup>8</sup>K. Gao, Q. Bi, X. Wang, W. Liu, C. Xing, K. Li, D. Xu, Z. Su, C. Zhang, J. Yu, D. Li, B. Sun, J. Bullock, X. Zhang, and X. Yang, *Adv. Mater.* **34**(26), 2200344 (2022).
- <sup>9</sup>X. Yang, Q. Bi, H. Ali, K. Davis, W. V. Schoenfeld, and K. Weber, *Adv. Mater.* **28**(28), 5891–5897 (2016).
- <sup>10</sup>F. Wang, S. Zhao, B. Liu, Y. Li, Q. Ren, R. Du, N. Wang, C. Wei, X. Chen, G. Wang, B. Yan, Y. Zhao, and X. Zhang, *Nano Energy* **39**, 437–443 (2017).
- <sup>11</sup>Y. Wan, S. K. Karuturi, C. Samundsett, J. Bullock, M. Hettick, D. Yan, J. Peng, P. R. Narangari, S. Mokkapati, H. H. Tan, C. Jagadish, A. Javey, and A. Cuevas, *ACS Energy Lett.* **3**(1), 125–131 (2018).
- <sup>12</sup>K. Li, K. Gao, X. Wang, X. Lou, D. Xu, C. Xing, W. Li, H. Li, and X. Yang, *Sci. China Mater.* **67**, 2866–2872 (2024).
- <sup>13</sup>Y. Wan, C. Samundsett, J. Bullock, M. Hettick, T. Allen, D. Yan, J. Peng, Y. Wu, J. Cui, A. Javey, and A. Cuevas, *Adv. Energy Mater.* **7**(5), 1601863 (2017).
- <sup>14</sup>K. Gao, W. Li, X. Chen, P. Xie, J. Zhou, C. Yu, J. Mao, P. Zheng, X. Zhang, and X. Yang, *Sol. Energy Mater. Sol. Cells* **282**, 113363 (2025).
- <sup>15</sup>C. Xing, W. Gu, K. Gao, B. Shao, C. Jiang, G. Bai, D. Xu, W. Xing, K. Li, Z. Song, Z. Su, J. Mao, X. Zhang, P. Zheng, W. Zhang, X. Zhang, Y. Wang, X. Yang, and B. Sun, *Sol. RRL* **7**(9), 2201100 (2023).
- <sup>16</sup>C. Xing, C. Jiang, W. Gu, W. Lou, K. Gao, Y. Song, B. Shao, K. Li, X. Wang, D. Xu, X. Zhang, Y. Wang, X. Yang, and B. Sun, *Prog. Photovoltaics Res. Appl.* **32**(1), 35–44 (2024).
- <sup>17</sup>K. Gao, C. Xing, D. Xu, X. Lou, X. Wang, K. Li, W. Li, J. Mao, P. Zheng, X. Zhang, and X. Yang, *Small* **20**(29), 2310352 (2024).
- <sup>18</sup>Y. Wan, C. Samundsett, J. Bullock, T. Allen, M. Hettick, D. Yan, P. Zheng, X. Zhang, J. Cui, J. McKeon, A. Javey, and A. Cuevas, *ACS Appl. Mater. Interfaces* **8**(23), 14671–14677 (2016).

- <sup>19</sup>X. Yang, W. Liu, M. D. Bastiani, T. Allen, J. Kang, H. Xu, E. Aydin, L. Xu, Q. Bi, H. Dang, E. Alhabshi, K. Kotovos, A. Alsaggaf, I. Gereige, Y. Wan, J. Peng, C. Samundsett, A. Cuevas, and S. De Wolf, *Joule* **3**(5), 1314–1327 (2019).
- <sup>20</sup>X. Yang, E. Aydin, H. Xu, J. Kang, M. Hedhili, W. Liu, Y. Wan, J. Peng, C. Samundsett, A. Cuevas, and S. De Wolf, *Adv. Energy Mater.* **8**(20), 1800608 (2018).
- <sup>21</sup>K. Gao, D. Xu, J. Wang, Q. Bi, Z. Wu, H. Lin, S. Wang, W. Shi, C. Yu, F. Cao, Y. Diao, J. Xie, X. Wang, K. Li, X. Lou, W. Li, C. Xing, Y. Wang, T. Yan, D. Zhang, S. De Wolf, X. Zhang, and X. Yang, *Adv. Funct. Mater.* **35**(4), 2415039 (2025).
- <sup>22</sup>D. Xu, Q. Bi, K. Li, K. Gao, X. Wang, W. Shi, S. Wang, C. Xing, X. Zhang, and X. Yang, *Adv. Funct. Mater.* **34**(44), 2407290 (2024).
- <sup>23</sup>C. Xing, W. Gu, Z. Xiang, X. Lou, X. Wang, X. Zhang, Y. Wang, X. Yang, and B. Sun, *Chem. Eng. J.* **481**, 148568 (2024).
- <sup>24</sup>J. Dréon, Q. Jeangros, J. Cattin, J. Haschke, L. Antognini, C. Ballif, and M. Boccard, *Nano Energy* **70**, 104495 (2020).
- <sup>25</sup>J. Li, T. Pan, J. Wang, S. Cao, Y. Lin, B. Hoex, Z. Ma, L. Lu, L. Yang, B. Sun, and D. Li, *ACS Appl. Mater. Interfaces* **12**(32), 36778–36786 (2020).
- <sup>26</sup>G. Du, L. Li, X. Yang, X. Zhou, Z. Su, P. Cheng, Y. Lin, L. Lu, J. Wang, L. Yang, X. Gao, X. Chen, and D. Li, *Adv. Mater. Interfaces* **8**(22), 2100989 (2021).
- <sup>27</sup>X. Yang, H. Xu, W. Liu, Q. Bi, L. Xu, J. Kang, M. N. Hedhili, B. Sun, X. Zhang, and S. De Wolf, *Adv. Electron. Mater.* **6**(8), 2000467 (2020).
- <sup>28</sup>M. Bivour, J. Temmler, H. Steinkemper, and M. Hermle, *Sol. Energy Mater. Sol. Cells* **142**, 34–41 (2015).
- <sup>29</sup>G. Du, L. Li, H. Zhu, L. Lu, X. Zhou, Z. Gu, S. Zhang, X. Yang, J. Wang, L. Yang, X. Chen, and D. Li, *EcoMat* **4**(3), e12175 (2022).
- <sup>30</sup>L. Li, L. Ying, Y. Lin, X. Li, X. Zhou, G. Du, Y. Gao, W. Liu, L. Lu, J. Wang, L. Yang, S. Zhang, and D. Li, *Adv. Funct. Mater.* **32**(43), 2207158 (2022).
- <sup>31</sup>L. Cao, P. Procel, A. Alcañiz, J. Yan, F. Tichelhaar, E. Özkel, Y. Zhao, C. Han, G. Yang, Z. Yao, M. Zeman, R. Santbergen, L. Mazzarella, and O. Isabella, *Prog. Photovoltaics Res. Appl.* **31**(12), 1245–1254 (2023).
- <sup>32</sup>J. Tian, K. Xu, G. Wang, H. Jiang, Y. Liu, P. Zhu, and D. Wang, *Appl. Phys. Lett.* **122**(11), 113903 (2023).
- <sup>33</sup>X. Yang, Y. Lin, J. Liu, W. Liu, Q. Bi, X. Song, J. Kang, F. Xu, L. Xu, M. N. Hedhili, D. Baran, X. Zhang, T. D. Anthopoulos, and S. D. Wolf, *Adv. Mater.* **32**(32), 2002608 (2020).
- <sup>34</sup>J. Yu, Y. Chen, J. He, Y. Bai, R. Su, T. Cao, W. Liu, and T. Chen, *Sol. Energy Mater. Sol. Cells* **260**, 112491 (2023).
- <sup>35</sup>M. Kot, K. Henkel, C. Das, S. Brizzi, I. Kärkkänen, J. Schneidewind, F. Naumann, H. Gargouri, and D. Schmeißer, *Surf. Coat. Technol.* **324**, 586–593 (2017).
- <sup>36</sup>G. K. Reeves and H. B. Harrison, *IEEE Electron Device Lett.* **3**(5), 111–113 (1982).
- <sup>37</sup>Z. Xin, Y. Ding, Y. Zhu, C. Fu, Z. Yao, Q. Chen, G. Liu, and F. Shan, *Adv. Electron. Mater.* **6**, 1901110 (2020).
- <sup>38</sup>J. Schmidt, B. Veith, and R. Brendel, *Phys. Status Solidi RRL* **3**(9), 287–289 (2009).